ELSEVIER

Contents lists available at ScienceDirect

Applied Ocean Research

journal homepage: www.elsevier.com/locate/apor



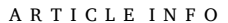
Research paper

Leveraging Distributed Acoustic Sensing for monitoring vessels using submarine fiber-optic cables

Bob Paap ^{a,b,*}, Vincent Vandeweijer ^a, Jan-Diederik van Wees ^{a,b}, Dirk Kraaijpoel ^a



^b Department of Earth Sciences, Utrecht University, Princetonlaan 8a, 3584 CB, Utrecht, the Netherlands



Keywords: Vessel traffic Distributed Acoustic Sensing Seabed infrastructure

ABSTRACT

The global offshore cable and pipeline infrastructure is ever growing to fulfill our demand for renewable energy -and internet communication. At the same time there is an increasing amount of vessel traffic due to the growth of offshore activities, which also imposes an increased risk of damage done to seabed infrastructure. This highlights the need to develop methods for continuously monitoring vessel traffic in the vicinity of seabed infrastructure over its full extent. Recent studies have demonstrated that redundant optical fibers pre-existing in offshore cables and pipelines (i.e., dark fibers), can be used to monitor vibrations along and over long distances (>100 km) using a Distributed Acoustic Sensing (DAS) interrogator. Different vessel parts are inducing acoustic vibrations, that subsequently propagate through the water column and shallow subsurface and temporarily deform a fiber-optic cable present inside seabed infrastructure. We developed a migration-based source location method to automatically detect and locate vessels using dark-fiber data and applied it both to a dataset acquired on the Dutch North Sea and a dataset from the west coast of Oregon, USA. The track, speed and course of the considered vessels determined from the analysis of DAS data show excellent agreement with the Automatic Identification System data in the vicinity of the fiber-optic cable. The migration-based source location method effectively uses the high spatial-temporal density of DAS data by constructive summation of coherent waveforms over space and time. Furthermore, the method can be extended to construct and refine velocity models by iteratively modifying the velocity model until a maximum of the objective function is found—corresponding to an optimal fit between observed and synthetic travel-times—provided that the uncertainty in propagation speed can be decoupled from position uncertainties in the fiber-optic cable. Thereby the method allows both for optimizing the velocity model and inverting for the acoustic source location in a sequential manner, which makes it additional valuable for subsurface studies.

1. Introduction

The increasing demand for renewable energy and internet communication has led to the rapid expansion of the global offshore cable and pipeline infrastructure. These underwater networks are vital for the energy supply and digital connectivity. In parallel, the rise in offshore activities such as wind farm operations, CO₂ storage, H₂ storage, hydrocarbon production and fisheries has resulted in a noticeable increase in vessel traffic. This significantly increases the risk of damage to seabed infrastructure, such as from vessel anchors dropped nearby or fishing trawlers operating in the area. This calls for the need for effective, affordable and full-scale continuous methods for monitoring marine

surface vessel traffic in the vicinity of seabed infrastructure.

The most relevant methods capable of detection and/or tracking surface vessels are Automatic Identification System (AIS) data, radar systems, and satellite imagery. AIS data can be an excellent source of vessel information, but this is not a definitive solution. Smaller recreational vessels are not always obliged to have an AIS transceiver, and some vessels may disable or spoof their AIS signals. Radar systems and satellite imagery are well-suited for scanning large areas with high spatial resolution at relatively low cost. However, satellite imagery can only be collected intermittently, therefore not allowing continuous monitoring. Furthermore, radar and satellite do not sense possible maritime activity below the sea surface close to infrastructure.

E-mail address: bob.paap@tno.nl (B. Paap).

https://doi.org/10.1016/j.apor.2025.104422

Received 25 October 2024; Received in revised form 20 December 2024; Accepted 6 January 2025 Available online 16 January 2025

0141-1187/© 2025 The Authors. Published by Elsevier Ltd. This is an open access article under the CC BY-NC-ND license (http://creativecommons.org/licenses/by-nc-nd/4.0/).

^{*} Corresponding author at: GeoScience and Technology, Netherlands Organization for Applied Scientific Research (TNO), Princetonlaan 6, 3584 CB, Utrecht, the Netherlands.

Table 1Characteristics of hardware, acquisition parameters and water depth for the Oregon and North Sea dataset.

Specifications	North Sea dataset	Oregon dataset
Acquired by	TNO in 2023	Wilcock and Ocean Observatories Initiative (2023)
Cable type	Export cable	Telecommunication cable
Interrogator type	FEBUS A1- LR	Optasense QuantX
Sampling frequency (Hz)	500	500
Gauge length (m)	30	30
Channel spacing (m)	5	2
Approximate water depth (m)	20	450

DAS is a relatively new acoustic data acquisition method that has been developing rapidly over the past years. An extensive description of the principles of DAS measurements is for instance presented by Hartog (2017), SEAFOM (2024). DAS measurements are acquired with a DAS interrogator connected to an optical fiber. The interrogator emits coherent laser pulses through the fiber, where each laser pulse is partially scattered back (i.e., Rayleigh backscattering) at very small inhomogeneities (nanometer scale) that pre-exist inside the fiber. The interrogator receives the back-scattered pulses and strain is determined from phase changes over a distance called the gauge length. Externally induced acoustic waves propagating through a medium will locally and temporarily apply axial strain to the fiber (i.e. along cable direction), which can be incidentally or continuously measured by the DAS interrogator over the full cable length.

DAS has become an attractive measurement technique complimentary to traditional point sensors (e.g., hydrophones, geophones). There are numerous examples where DAS has successfully been used for (timelapse) subsurface imaging for hydrocarbon production, geothermal, $\rm CO_2$ Storage sites, as well as for earthquake monitoring (e.g., Mestayer et al., 2012; Mateeva et al., 2013; Dean et al., 2017; Wang et al., 2018). DAS data-acquisition has the advantage that fibers are cost-attractive and that a very high spatial data density can be reached over long cable distances in contrast to localized point sensors. Moreover, extended DAS interrogator types have become available that can conduct measurements on fibers in co-existence with telecommunication traffic (i.e. lit fibers).

Various research groups have demonstrated the use of DAS for interrogating pre-existing fibers (i.e., dark fibers) in seabed infrastructure, including studies on earthquakes and subsurface characterization (Jousset et al. 2018; Lindsey et al., 2020; Landrø et al., 2022), environmental noise and ocean waves (Williams et al., 2019; Landrø et al., 2022), and marine mammals (Bouffaut et al., 2022; Landrø et al., 2022). Dark fibers are also recognized as promising complimentary approach for monitoring marine vessels near subsea infrastructures more effectively, since measurements can be conducted utilizing redundant fiber-optic fibers within existing offshore cables and pipelines. This potential has been recently demonstrated by several authors (Rivet et al., 2021; Landrø et al., 2022; Wilcock et al., 2023, Thiem et al., 2023; Drylerakis et al., 2024). Landrø et al. (2022), Bouffaut et al. (2022) used a cross-correlation approach to locate acoustic source respectively of a vessel and of whales as recorded on dark fiber data. Specifically, the approach of Thiem et al. (2023) focused on the enhancement of coherent signal through data denoising and subsequent source location by minimizing the misfit between observed and synthetic travel times, while only accounting for direct waves (i.e. waves directly travelling from source to receiver through the water layer). Alternatively, Drylerakis et al (2024) present a machine learning based approach to detect and locate vessels, using an unsupervised dimensionality reduction technique based on principle component analysis. Challenges for vessel monitoring mainly rely in (1) optimizing data quality, which is

dependent on the hardware specifications and acquisition settings of the interrogator, (2) tailoring processing algorithms to extract vessel specific characteristics from DAS-data, and (3) effectively handling large data streams of continuously acquired DAS data to facilitate (near) real-time data processing and dissemination. The data quality of DAS data depends on various factors including the cable design (type and embedding of fiber), cable coupling conditions, cable burial conditions, environmental noise (e.g., sea state, anthropogenic noise), and the performance of the used DAS interrogator. Specifically, when using dark fibers from already existing infrastructure to acquire DAS data the cable design and cable deployment condition is simply accepted without any external interference, such that the quality and value of the data can only be optimized by tuning the hardware components and the acquisition settings of the DAS interrogator, and by developing dedicated data-processing workflows.

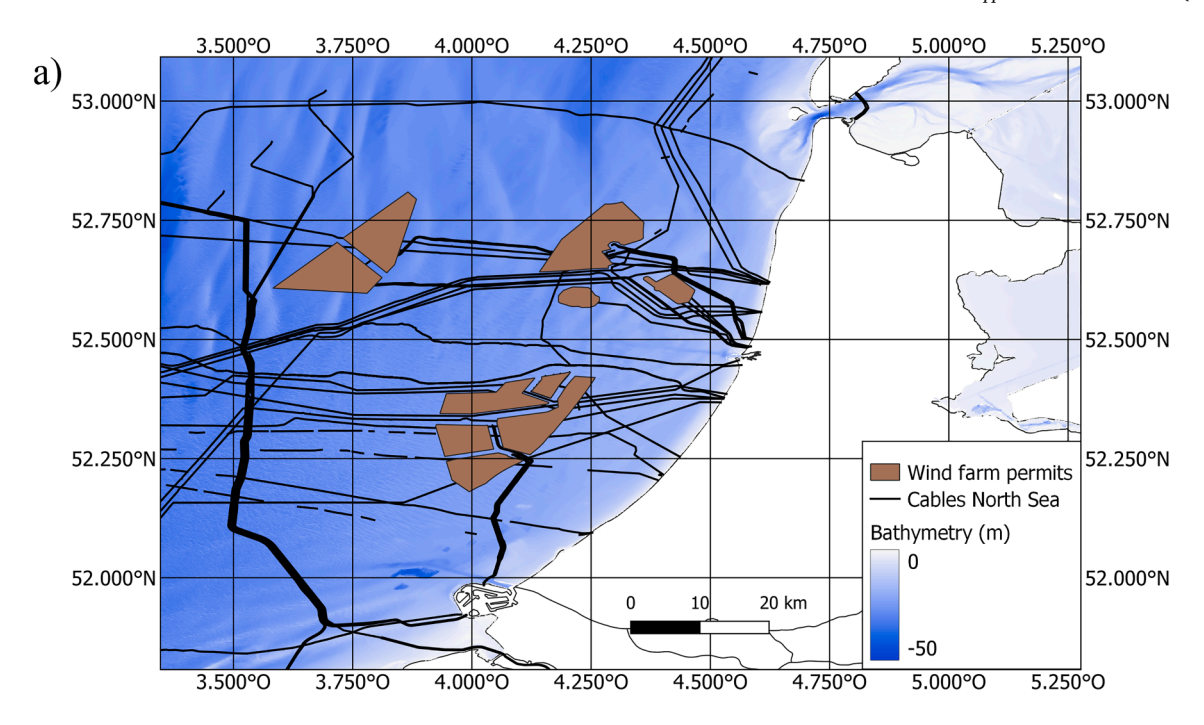
This study focuses on the automatic detection and localization of vessels near submarine fiber-optic cables using distributed fiber-optic sensing employing a methodology that incorporates noise suppression, migration-based source location, and k-means clustering. To evaluate its performance, the methodology is applied to DAS data from two contrasting sources: a seabed cable transporting power generated by a wind farm (i.e., an export power cable) in the Dutch North Sea, and a telecommunication cable located off the west coast of Oregon, USA. These datasets differ significantly in terms of the DAS interrogator used, cable types (export power versus telecommunication cable), considered vessel types, water depths (shallow versus deep waters), and noise conditions (absence versus presence of surface gravity waves). These diverse conditions make the evaluation particularly interesting, as they highlight the methodology's adaptability and robustness across varying scenarios. Additionally, we use the migration-based source location algorithm to optimize the velocity of the top sediment layer, ensuring accurate modeling of the refracted wave travelling through the sediment layer. This optimization, in turn, enhances the precision of the acoustic source localization.

2. Datasets

Two datasets were considered in this study; the first acquired by the authors on an export cable running to an offshore windfarm on the Dutch North Sea, and the second being a publicly available dataset acquired at the West coast of Oregon (USA) by Wilcock and Ocean Observatories Initiative (2023). The specifications of the two datasets are listed in Table 1.

2.1. North Sea dataset

The North Sea data was acquired using a FEBUS A1-LR DAS interrogator connected to a fiber-optic cable, part of the export cable connecting an offshore windfarm to shore. The windfarm is situated of the west coast of the Netherlands in the North Sea. Because of confidentiality reasons the location of the specific cable cannot be shared. Fig. 1 does show an overview of submarine cables, including export cables from windfarms, in the Dutch North Sea, as well as the areas where wind farm permits are assigned. Export cables from windfarms are usually covered by a few meters of sediment. The North Sea DAS data was acquired over the full length of the export cable (approximately 33 km long) over an eight-day period in October 2023. The data was sampled at 500 Hz with a 30 m gauge length and 5 m channel spacing and retrieved in strain rate (see Table 1). The total data volume amounted to approximately 20 TB. There is extensive vessel traffic in this area of the North Sea. During the DAS measurement campaign, we simultaneously collected publicly available AIS data, providing real-time positions of vessels in the area near the interrogated export cable. The study area is characterized by shallow water depths of approximately 20 m and wave heights reaching around 2 m, during the period of acquisition. The cable has an average burial depth of 2 m and was predominantly overlain by



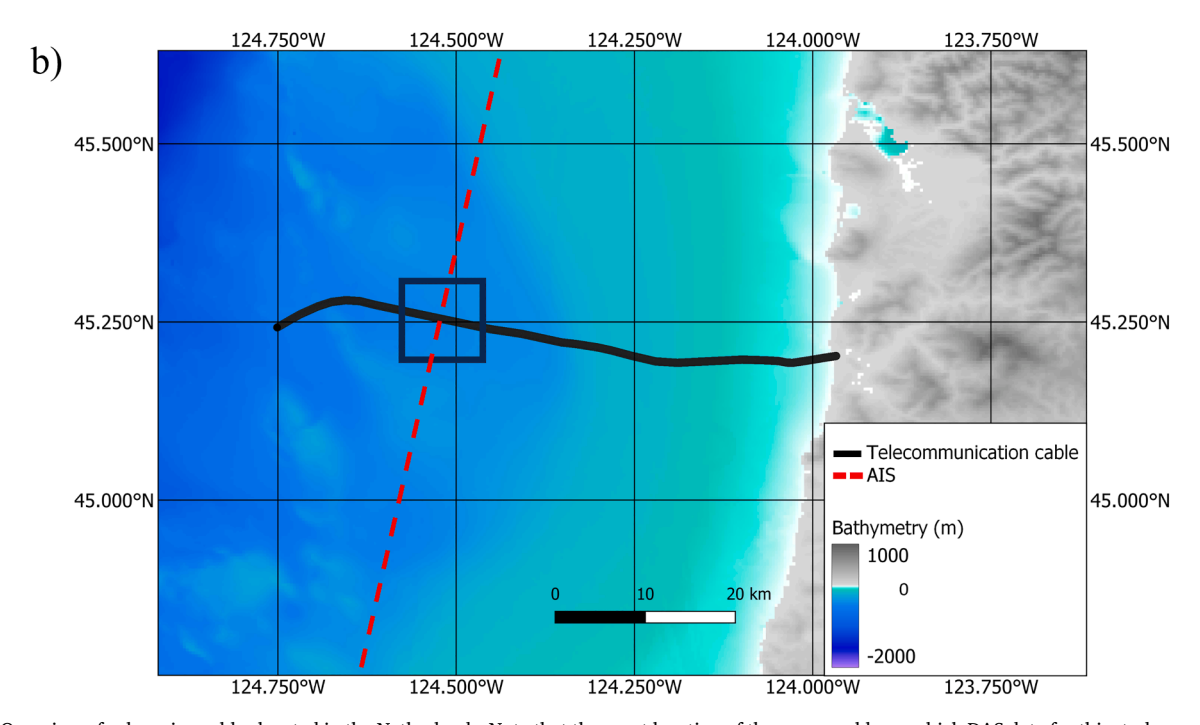


Fig. 1. (a) Overview of submarine cables located in the Netherlands. Note that the exact location of the power cable on which DAS data for this study was acquired is confidential and cannot be reported. Bathymetric data is obtained from Emodnet (2025). Cable location information and data of wind farm permit zones are obtained from Rijkswaterstaat (2025) https://maps.rijkswaterstaat.nl. (b) Location of submarine telecommunication cable (black) and the considered vessel's track (red) situated west of Oregon, USA (see source data from Wilcock and Ocean Observatories Initiative (2023)). Bathymetric data was obtained from General bathymetric Chart of the Oceans (Gebco, 2025) https://www.gebco.net/. Coordinates of Fig. 1a and b are both plotted in WGS' 84 in degrees.

moderate to coarse sand.

2.2. Oregon dataset

Wilcock et al. (2023) acquired DAS data on a telecommunication cable and published the observation of a passing cargo vessel (see Fig. 1 and Table 1). We used the DAS data acquired during the passage of the vessel over the cable. The track of the cargo vessel was reconstructed from the course over ground and speed over ground as reported by

Wilcock et al. (2023), and by using the approximate cable passage point of the vessel as observed on the DAS data. The water depth in the area of interest is approximately 450 m and the average cable burial depth is 1.5 m (Wilcock et al., 2023).

3. Methodology for automated vessel tracking based on DAS

The key-objective was to detect and locate acoustic signals resulting

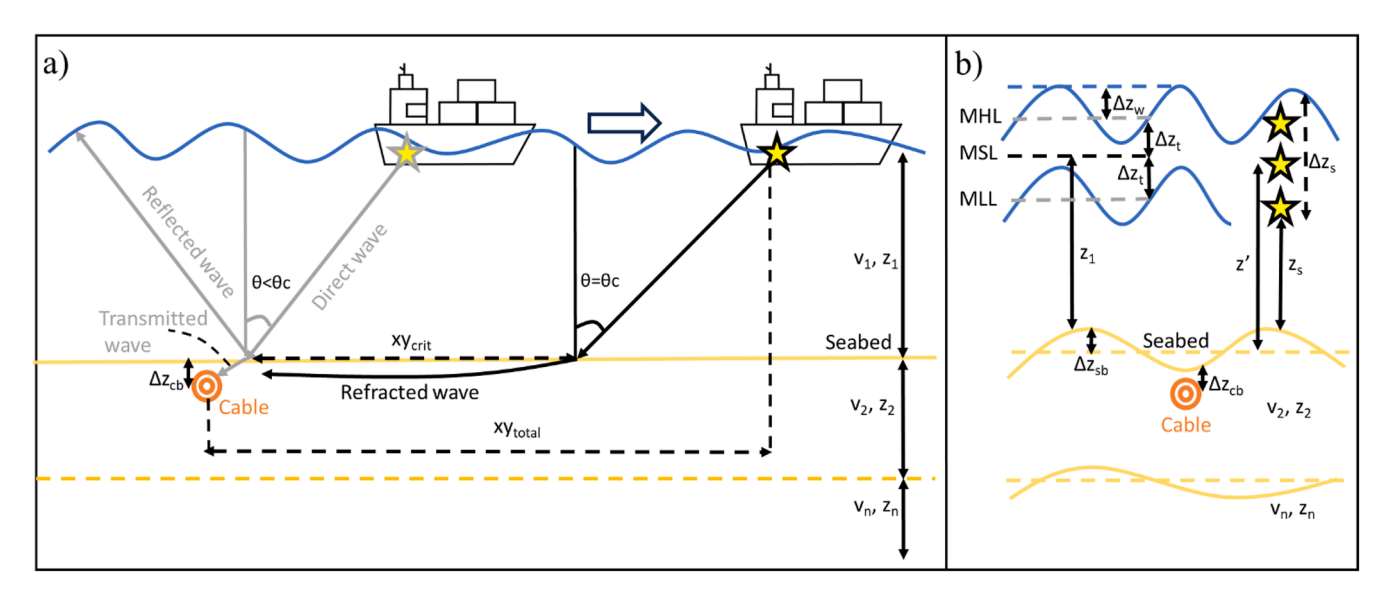


Fig. 2. Illustrations of the relevant wave types and geometrical aspects for vessel-induced acoustic waves recorded by a fiber-optic cable near the seabed. (a) Different vibrating vessel parts of are here simplified as a composed acoustic point source (yellow star) that result in a direct acoustic wave travelling (grey arrow) through the water column (z_1) when the angle of incidence is smaller than the critical angle. Upon arriving at the seabed, the direct wave is partially converted in a reflected wave and partially in a transmitted wave (grey arrows) travelling through the shallow subsurface to the buried fiber-optic cable (orange). When the angle of incidence equals the critical angle, the direct wave is converted to a refracted wave travelling through the sediment layer towards the cable. See main text for further explanation. (B) Geometrical altitude aspects that affect the acoustic wave paths and which had to be partially simplified due to a lack of data and to reach a feasible methodological implementation. See main text for further explanation.

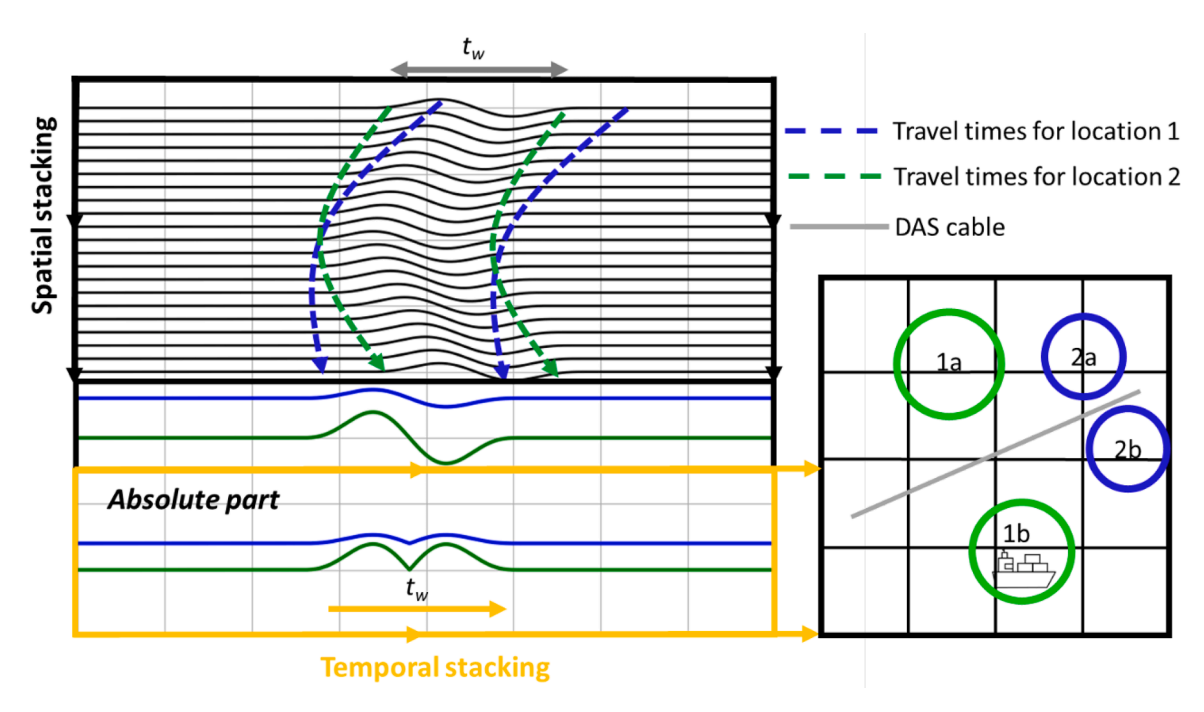


Fig. 3. Concept of the migration-based source location method. First travel-time curves are calculated for different source-receiver pairs. Here, sources and receivers respectively correspond to possible acoustic source (i.e. vessel) locations (blue and green circles on grid) and DAS receivers along the fiber-optic cable (grey line). Next, recorded DAS waveforms are stacked (i.e. summed) over the spatial dimension (black arrow) within a pre-defined time window along the pre-calculated travel time curve corresponding to the synthetic source locations on the grid at the right (green and blue). Finally, the absolute part of the resulting signal is stacked over the time dimension (orange arrow) which results in a single positive stacking value per source location. The location with the highest stacking value as indicated with the proportionally larger green circle, represents the most likely location of the actual acoustic source generated by a vessel. With DAS measurements only strain is sensed in the axial direction making it a single-component measurement. This results in ambiguity in the estimated source location, with two possible source locations symmetrically positioned on both sides of the fiber-optic cable (1a and 1b). Note that for the real application we employ a full grid search.

from vessels in the vicinity of the considered seabed cables. The various components of a vessel (e.g., propellors, engines, pumps, generators) induce hydroacoustic waves at particular frequency bands (Malinowski, 2001; Żak, 2008; Chung et al., 2011). These acoustic waves can be

sensed by a DAS interrogator.

Table 2 Characteristics of different vessel types considered in this study.

Aspect	North Sea dataset		Oregon dataset
Vessel type	1. Tugboat	2. LPG vessel	3. Cargo vessel
Length (m)	59	118	180
Speed (knots)	3.2	14.0	13.2
Assumed vertical source-receiver distance (m)	15	15	450
Distance along cable where vessel passed (m)	24250	19600	48750

Table 3Data processing- parameters and aspects relevant for the considered North Sea and Oregon datasets.

Processing phase	Processing	North Sea dataset	Oregon dataset
Preprocessing	Taper to suppress edge effects	-	Tukey
	Bandpass filter	15-240 Hz	5-100 Hz
	FK-filter (low- and high-end	1400-3500	1400-
	slope)	m/s	15100 m/s
Migration-based source location	Velocity in sea water velocity $-v_1(m/s)$	1500	1500
	Velocity in upper subsurface layer -v ₂ (m/s)	1700	1550
	Critical distance (m, see Eq. (2))	28	1728
	Grid size - x/y (m)	4000/ 4000	5000/6000
	Grid point spacing	$10\times10\ m$	$20\times20\;m$
	Length of used cable segment	2000 m	4000 m
	Stacking window for migration-based source location	1.0 s	1.0 s

3.1. Considerations for fiber-optic monitoring of vessel-induced acoustic waves

The concept of the most relevant acoustic wave types induced by a vessel and geometrical aspects is presented in Fig. 2. We assume the various vibrating parts of a moving vessel can be simplified as a composed point source (yellow star in Fig. 2a), which is valid for farfield observations. Out of practical reasons we extend this point source approximation to the near-field, which we are also observing and neglect the actual volume in which different acoustic sources exist that correspond to different parts of the vessel. For small-receiver offsets the considered acoustic waves will travel as straight direct waves with the water sound velocity v_1 to the seabed (grey downward arrow in Fig. 2a), where it is converted in an upward reflected- and downward transmitted wave (grey arrows). If the cable is exposed, the direct wave will reach it, whereas when buried, the transmitted wave will penetrate and reach it. When the angle of incidence exceeds the critical angle, direct waves will solely be converted to refracted waves traveling through the top layer of the subsurface with velocity v_2 to the cable (black arrow in Fig. 2).

The critical angle θ_c is given by Snell's law:

$$\theta_c = \operatorname{asin}\left(\frac{v_1}{v_2}\right) \tag{1}$$

The corresponding critical distance(xy_{crit}) at which refracted waves originate that travel through the sediment (in the remainder of this work referred to as refracted wave), can be geometrically deduced from the water depth (z_1) and defined by:

$$xy_{crit} = z_1 * \tan(\theta_c)$$
 (2)

The travel time $T(x_r, y_r, z_r)$ of the direct wave from source (s) to

receiver (r) can be expressed in 3D space as:

$$T(x_r, y_r, z_r)_{direct} = \frac{\sqrt{(x_r - x_s)^2 + (y_r - y_s)^2 + (z_r - z_s)^2}}{v_1}$$
(3)

And the travel time of the refracted wave as:

$$T(x_r, y_r, z_r)_{refracted} = \left(\frac{z_2}{v_1 * \cos(\theta_c)}\right) + \left(\frac{xy_{total} - xy_{crit}}{v_2}\right)$$
(4)

Where

$$xy_{total} = \sqrt{(x_r - x_s)^2 + (y_r - y_s)^2}$$
 (5)

Note that in practice, for shallow-buried cables surrounded by unconsolidated sediments, the direct wave may still be observed in DAS measurements to some extent at distances beyond the critical distance. It is essential to highlight the role of various geometrical variables and their associated uncertainties in the context of our field application (i.e. dark fiber data-acquisition of vessel-induced acoustic waves). Oceans can be highly dynamic systems, which especially holds for the Dutch North Sea, where dynamic bedforms exist at the seabed with different spatial characteristics. This includes tidal sand waves that can reach heights over 5 m and are highly mobile with lateral movements of tens of meter per year (Cheng et al., 2020). Both bathymetrical charts and measurements of cable burial depth data are periodically acquired, typically at a minimum of 1 year interval due to associated costs. Therefore, as illustrated in Fig. 2b, the reported cable burial depth (Δz_{cb}) and bathymetry (z_1) have limited reliability given the dynamic nature of the seabed (Δz_{sb}). Also, uncertainty is associated with the vessel source depth (Δz_s), that results from (1) short period ocean wave height variations (Δz_w), (2) the position of the active acoustic source region which depends on design and draught of a vessel, and (3) tidal variations (Δz_t) at the location of the considered DAS cable segment.

Given these unknowns and uncertainties we simplified the geometry by approximating the vertical source-receiver distance as:

$$z' \approx z'_1 - (\Delta z'_{cb} + \Delta z'_{s})$$
 (6)

With $\mathbf{z'}_1$ the mean bathymetric depth, $\Delta \mathbf{z'}_{cb}$ the mean cable burial depth and $\Delta \mathbf{z'}_s$ an estimate of the depth of the vessel's source region $(\Delta \mathbf{z'}_s)$.

We also made several assumptions concerning the role of other acoustic waves. We neglected the contribution of the small extra path from seabed to cable as travelled by the transmitted wave and assumed that below the critical distance the total travel time can be approximated by only considering the path of the direct wave (see Eqs. (2) and (3)). We assume that above the critical distance the first arrival reaching the cable is given by the refracted wave as given (Eq. (4)). Additionally, other converted wave types will originate and be recorded on the cable with DAS measurements. At relatively small source-receiver offsets, subsurface reflections, subsurface multiples and water multiples will be continuously generated. At larger source-receiver offsets refractions and reflections will originate in the deeper subsurface. Although these various wave types will be recorded as well with DAS measurements, we neglected them to reach a simplified representation of primary arrivals within the migration-based source location method, as described next.

3.2. Migration-based source location method

Because DAS data can have relatively high noise levels (especially on dark fibers) as well as an extensive data-volume, we needed an efficient and robust detection- and location method for acoustic events. We anticipated that especially the North Sea dataset could suffer from higher noise levels due to its shallow waters (\sim 20 m) and often turbulent sea state. Here wave heights can reach 4 m during a wind force 7 on the Beaufort scale. The combination of these wave heights with shallow water depths, results in significant water pressure variations

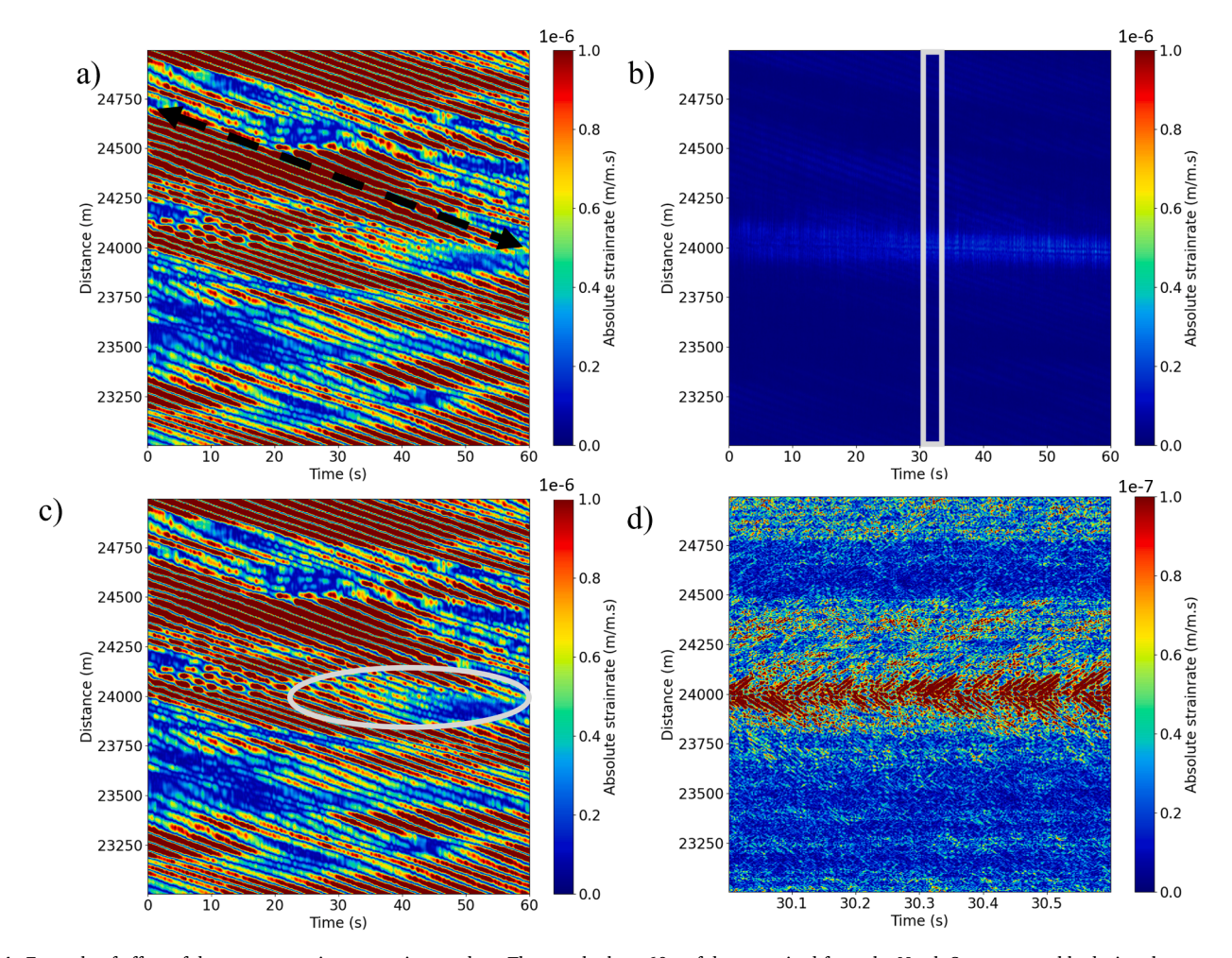


Fig. 4. Example of effect of data preprocessing on strain rate data. The panels show 60 s of data acquired from the North Sea export cable during the passage of a tugboat (see Table 2). (a) Raw strain rate data showing the imprint of ocean surface gravity waves on the fiber-optic cable as indicated by the black dashed arrow. (b) Pre-processed strain rate data. See Table 3 for processing parameters (c) Difference between preprocessed- and raw strain rate data where subtle differences are highlighted by the grey ellipse. (d) Close-up of the preprocessed data within the time window highlighted by the grey rectangle in b, showing the clear presence of the vessel-induced acoustic event. Note that we plotted the absolute strain rate to enhance data visualization.

applied to the seabed and underlying cable. These pressure variations result in considerable strain changes on the cable and further increase the noise levels on the DAS data.

Various automated methods exist for detecting seismic events, which are equally applicable to acoustic events. This includes detection based on short term averaging/long term averaging (STA/LTA) in the time or frequency domain (Vanderkulk et al., 1965, Withers et al., 1998), radon transform based (Butcher et al., 2021), cross-correlation with template waveforms (Gibbons and Ringdal, 2006) and machine learning based detection and location approaches (e.g. Curilem et al., 2009; Doubravová et al., 2016; Tiira, 1999, Shen et al., 2020; Alvaro et al., 2021; Anikiev et al, 2023; Drylerakis et al. (2024)). Here, an unsupervised neural network approach can offer an efficient way to detect and locate acoustic events (Drylerakis et al., 2024). Thiem et al. (2023) presented a workflow focusing on tracking vessels using DAS data, that consists of noise suppression, image enhancement to identify coherent signals, persistent homology to verify if the coherent signal corresponds to a direct wave and subsequent traveltime inversion by fitting polynomials to coherent signals to estimate the source location. Here, they only considered direct waves originating from the vessel and traveling through the water layer. Results for the considered vessel show its position can be reasonably estimated, although the method does not allow reconstruction of its full continuous track.

In this study, a migration-based source location method was implemented (Gharti et al., 2010; Smith et al., 2020; Winder et al., 2020),

which is also known as diffraction stacking or waveform stacking and migration. This method has strong similarities to beamforming as commonly used to process radar data (Yongtan, 1996; Chen et al., 2021; Cahl et al., 2023.), as well as to semblance-based velocity analysis as used in active seismic data processing (Gan et al., 2015). The migration-based source location method constructively combines coherent waveform data from an array, in our case a fiber-optic cable on which DAS data is acquired, and back-projects it to determine the source location. It has the advantage that weaker coherent signals in more noisy data are enhanced through constructive summation enabled by DAS's high spatial channel density, and that it can be applied in a fully automated fashion.

The method is presented in Fig. 3, where individual time samples of recorded trace data are first stacked (i.e. summed) in the spatial dimension along precalculated travel time curves for source-receiver pairs (obtained with Eqs. (3) and (4)). This operation is conducted for a series of time samples within a pre-defined time window t_w for all considered traces and basically results in a single stacked signal for each grid point (see Fig. 3). In turn the absolute part of this stacked signal is stacked along the time dimension resulting in a single stacked value per grid point (see Fig. 3). This operation can be expressed by the following objective function:

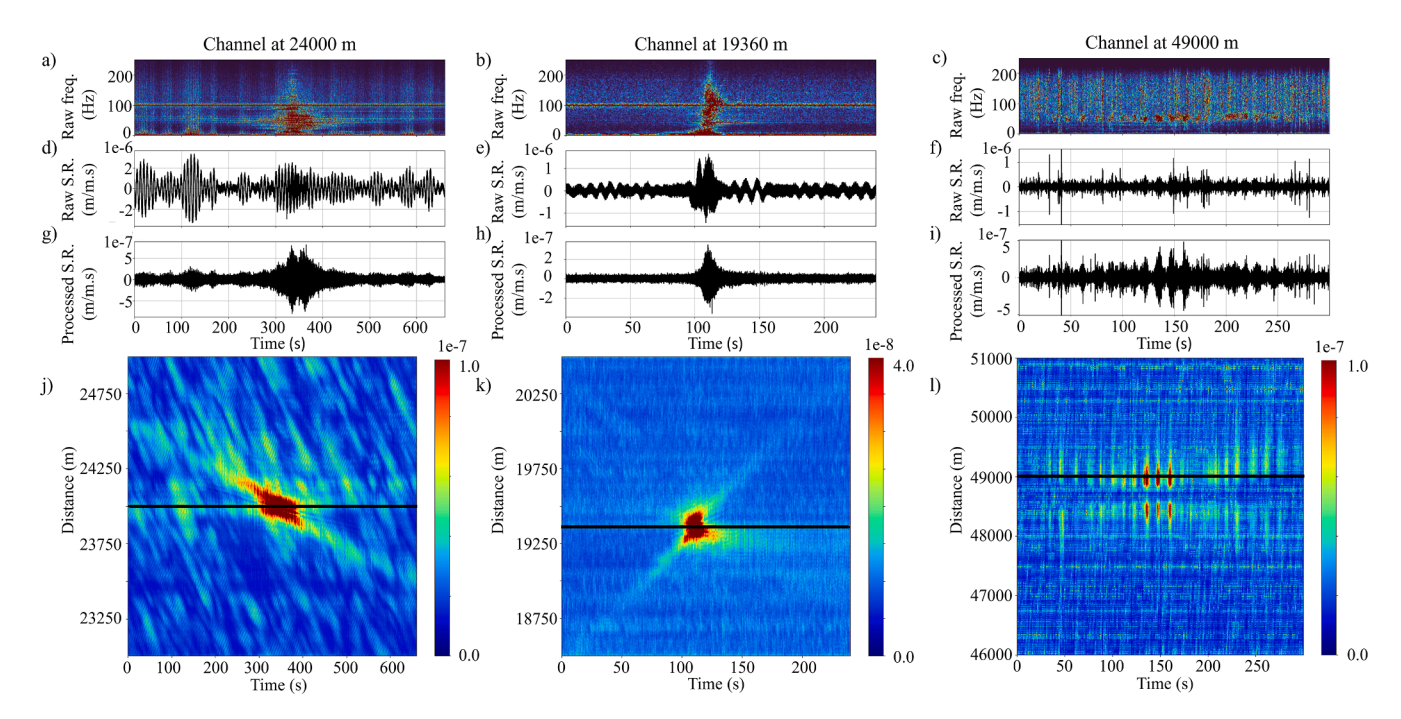


Fig. 5. The DAS strain rate as recorded by the DAS interrogator system for the three vessels considered in this study. (a, d, g, j) Tugboat passing the export cable at the North Sea site; (b, e, h, k) LPG vessel passing the export cable at the North Sea site; (c, f, i, l). Cargo vessel passing the telecommunication at the Oregon site. For each considered vessel passage we selected a DAS channel from which we plotted the time-frequency panels in a-c, the raw strain rate data in d-f, the processed strain rate data in g-i. The absolute strain rate data as a function of time and distance along the cable is plotted in j-l. Panels j-l also show the position of the selected channels that were plotted in a-i by the solid black line. The response on the DAS cable due to the passing vessels is clearly visible in j, k and l as indicated by dark red colors. For further details on the considered vessels, properties of the datasets and the conducted DAS data processing respectively see Tables 1-3.

$$S(\mathbf{x}) = \sum_{t=0}^{t_w} \left| \sum_{n=0}^{N-1} r_n(t + T_n(\mathbf{x})) \right|$$
 (7)

Where S(x) is the objective function for the position vector $\mathbf{x} = (x,y,z)$ at the source grid, and $T_n(\mathbf{x})$ is the travel time from source position \mathbf{x} to receiver n (given by Eqs. (3) and (4)). Furthermore r_n is the recorded sample at time t for receiver n, N is the total number of considered receivers, and t_w defines the selected time window within which the time series is stacked. When a coherent signal from an acoustic source is present within DAS data in a specific time window, the position vector \mathbf{x} of the source is identified as the location where the objective function $S(\mathbf{x})$ in Eq. (7) reaches its highest values. Note that in Fig. 3 the vessel-induced signal is simplified with a duration corresponding to a single wavelength, whereas in reality it is a continuous signal as the vessel constantly generates acoustic vibrations. We implemented a full-grid search where the objective function is calculated for all grid points in the considered area of interest.

In case there is an acoustic source at a specific location, this will result in the constructive summation of waveforms along the traveltimes for the respective source-receiver pairs, which in Fig. 3 is illustrated by the high stacking value found for the vessel at the position of the green circle. This process enhances coherent signals (those aligned with the travel time curves) while attenuating incoherent noise. The result from the objective function (Eq. (7)) can be visualized in an intensity heatmap, with stacking values corresponding to the relative likelihood of the location of coherent signals (e.g. blue and green circles in Fig. 3). Similar to linear hydrophone arrays, DAS arrays do not allow differentiation from which side of the cable signal arrives resulting in two possible locations, as indicated in Fig. 3 by the mirroring of the blue and green dots around the cable. To calculate source locations, we adopted k-means clustering imposing two clusters and applied it to the spatial occurrence of the 10 highest stacking values from the heat map obtained from Eq. (7). The selection of these 10 highest stacking values, corresponding to 10 position vectors x in Eq. (7), was based on initial

testing of the k-means clustering method, which demonstrated that this number effectively represents the region of the estimated source location. This results in two clusters, where in turn we took the mean location of each cluster as two final locations per analyzed data-block. We run the corresponding code on a high-performance cluster to efficiently process large volumes of successive DAS datafiles.

4. Results

During the research various vessels were detected, localized and identified. We consider the raw and processed DAS data and the outcome of the location algorithm for two vessels passing the export cable in the Dutch offshore and one vessel passing the telecommunication cable offshore the USA. Specifications of the considered vessels are indicated in Table 2, which shows variation in type, length, speed and water depth at the specific cable crossing location.

4.1. DAS recordings of vessel induced acoustic events

The DAS data was pre-processed to increase the signal to noise ratio, by applying a bandpass filter and successive frequency-wavenumber (FK) filter with settings prescribed in Table 3. As shown in Table 3, the optimal parameter settings differed between the two datasets, due to differences in their data- and signal characteristics. The settings for the bandpass filter and FK-filter were determined through initial data inspection and parameter testing. This showed that for the North Sea dataset vessel related signal was still present at relatively high frequencies compared to the Oregon dataset. Therefore, we used a higher high-cut value for the bandpass filter for the North Sea dataset than for the Oregon dataset. Also, for the Oregon dataset vessel related signal was identified in the FK spectrum at relatively high apparent velocities compared to the North Sea dataset. Therefore, we used a higher upper bound for the FK-filter for preprocessing of the Oregon dataset compared to the North Sea dataset, as shown in Table 3.

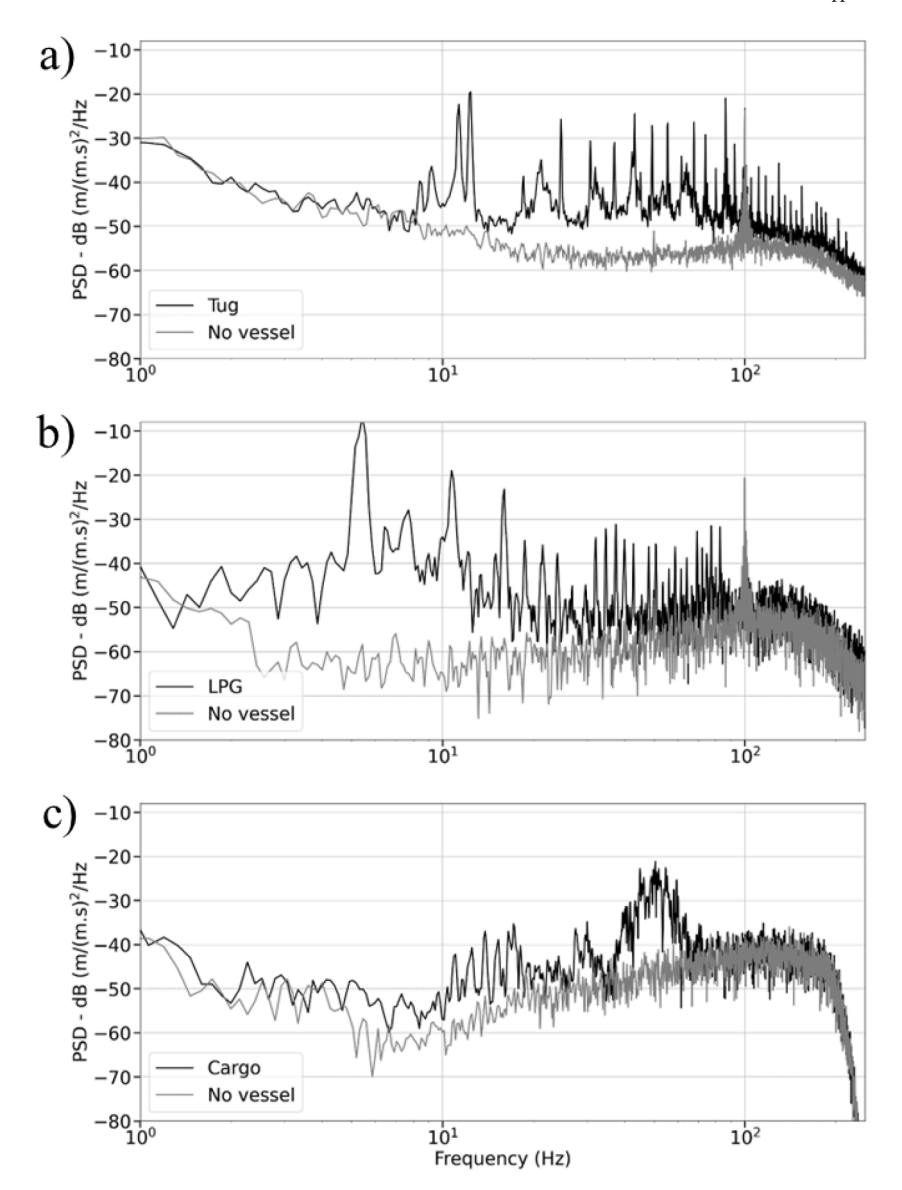


Fig. 6. Power spectral density plots for three raw DAS recordings corresponding to the three considered vessels (black) against background noise (grey). (a) North Sea Tugboat, (b) North Sea LPG vessel, (c) Oregon Cargo vessel. Here, the same DAS channels were selected for the three vessels as the reference channels highlighted by the black lines in Fig. 5 j—l. The DAS data time window for each case was chosen to correspond to approximately 100 m of vessel travel over the fiber-optic cable, based on the reported GPS position and speed over ground. Background noise data was evaluated at the same fiber-optic cable segment where each vessel passed, acquired an hour before the vessel passage. In each individual subplot the PSD of vessel and noise data are both normalized by the maximum PSD value of the respective vessel data.

Fig. 4 shows a comparison of absolute strain rate data as a function of time and distance for the North Sea dataset at the time a tugboat passed over the cable (see Table 2 for details on the vessel). Fig. 4a shows that the combined effect of ocean surface gravity waves and shallow water depths encountered at the North Sea causes significant water mass variations acting on the fiber-optic cable. The direction of the ocean surface gravity waves is marked by the black dashed arrow with an estimated apparent wave speed of approximately 11.8 m/s. Fig. 4b shows that we could significantly reduce the ocean gravity wave imprint using the afore mentioned pre-processing steps. Fig. 4c reflects the difference between preprocessed and raw strain rate data with subtle differences highlighted by the grey ellipse. Fig. 4d shows a close-up on a time window of Fig. 4b (marked by grey rectangle) with a clear presence of the vessel-induced acoustic event.

The recorded DAS data of the different vessels is shown in Fig. 5. Fig. 5a-c and Fig. 5 d-f, respectively show time-frequency and time domain waveform plots of raw strain rate data corresponding to a

selected DAS channel. Fig. 5 g–i shows the result of application of the pre-processing on the raw time signals from Fig. 5 d–f. Fig. 5j–l show the absolute strain rate as a function of time and distance along the cable, clearly depicting the DAS response due to acoustic waves generated by the considered vessels. Fig. 5j–l show the position of the DAS channels that was selected for the plots in Fig. 5a–i, as indicated by the black horizontal lines.

Fig. 5 shows that the acoustic signals generated by the considered vessels are more clearly defined for the North Sea- than for the Oregon dataset. For the North Sea data, the time-frequency plot (Fig. 5a and b) shows a finite and broadband response at the time the vessels passed as well as a clear response on the pre-processed time domain waveform data (Fig. 5 g and h). For the Oregon data the response of the passing vessel is weaker as expressed on the time-frequency and time waveform plots of the single channel visualization (Fig. 5 c, f and i). The signal shows periodic amplitude amplifications and attenuations (Fig. 5 i and l) whereas the DAS data for the North Sea vessels show a more gradual

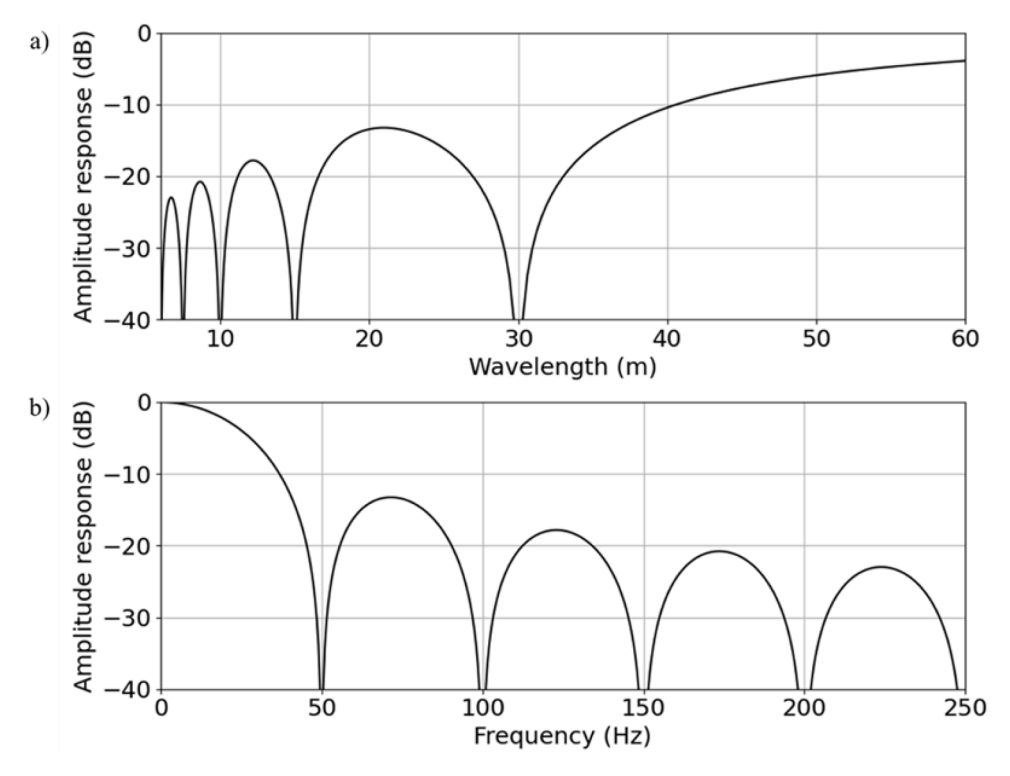


Fig. 7. Theoretical DAS amplitude response according to Eq. (8) based on a propagation velocity of 1500 m/s and gauge length of 30 m which are representative for the datasets considered in this study. (A) DAS amplitude response as a function of wavelength. (B) DAS amplitude response as a function of frequency.

strengthening and weakening when a vessel approaches and leaves the cable (Fig. 5 g and h). This might be related to a stronger effect of ocean waves on vessel movements for the Oregon case, resulting in spatial oscillations of the radiated wavefield. Also, the intensity plot for the Oregon case (Fig. 5l) shows a zone with a very weak response (blue zone at about 48,700 m cable length), which is probably caused by the vessel approaching the cable from an orthogonal direction. In this specific case, no acoustic signal is detected at the cable segment where the vessel crosses due to the cable's lack of sensitivity in the radial direction of the cable.

Fig. 6 presents a comparison of the power spectral density (PSD) expressed in dB for the raw DAS recordings of the three considered vessels (black) against the background noise (grey). Here, both the vessel and noise data spectra are normalized by the maximum spectral value of the respective vessel data in each subplot of Fig. 6. This normalization highlights the differences in frequency characteristics between the vessel-generated signals and the background noise. The time window selected to calculate the PSD of the background noise data was set equal to the time window of the corresponding selected vessel data. Based on the AIS data we selected a specific time window of the DAS data for each considered vessel, representing approximately 100 m of the vessel's travel over the fiber-optic cable. Background noise data was gathered from the same fiber-optic cable segment one hour before the vessel passed, such that the sea state can be assumed approximately constant while comparing data from identical cable segments.

The PSD curves of the considered vessel data recordings (black) is significantly higher compared to the background noise (grey) in Fig. 6. Various narrow frequency bands with increased magnitude are observed for the North Sea vessels (Fig. 6a and b). These likely represent characteristic frequencies of acoustic waves induced by the mechanical vibration of different vessel parts, which can be relevant for further vessel classification (Malinowski, 2001; Żak, 2008; Chung et al., 2011). More extensive research is needed to determine the precise cause of these frequency peaks and its potential use for vessel classification. Furthermore, a 100 Hz peak is observed on the North Sea data (Fig. 6a and b),

possibly induced by the alternating current inside the power cable. When inspecting smaller time windows of the North Sea- and Oregon datasets, the acoustic signatures of the considered vessels show similar hyperbolic shaped travel-time delays as a function of distance as illustrated in Fig. 8 a and c.

4.2. Application of migration-based source location algorithm

The parameters used for the migration-based source location method are listed in Table 3, which shows we assumed a velocity $\nu 1$ of 1500 m/s for the water layer in both datasets. This is a standard representative value for water, though the true velocity can vary depending on salinity and temperature.

The DAS cable response is affected by the spatial sampling settings of the considered datasets and related to the gauge length R_{gl} . Following Eq. (10) by Näsholm et al. (2022), the DAS cable response can be approximated by:

$$R_{gl}(\lambda) = \frac{1}{G} \left| \frac{\sin (\pi G/\lambda)}{\pi/\lambda} \right| \tag{8}$$

Where G is the gauge length and λ the wavelength. As shown in Table 3, the considered datasets have a gauge length (G) of 30 m. Assuming an average propagation velocity of 1500 m/s, Eq. (8) predicts the DAS response will decrease for wavelengths (λ) of 30 m and shorter and frequencies of 50 Hz and higher. This is illustrated in Fig. 7, showing the normalized DAS response as a function of wavelength (a) and frequency (b), with notches occurring at integer multiples of 50 Hz. Still, as shown in Fig. 6 the frequency response of the DAS recordings of the vessels clearly shows vessel-related energy (black) above 50 Hz when compared against the background recordings (grey). Furthermore, while doing initial tests, the outcome of the migration-based source location algorithm showed a clear improvement when including higher frequencies (above 50 Hz), because this further contributed to constructive summation of coherent signal. Since our goal was to maximize the performance of the location algorithm we preserved higher frequencies

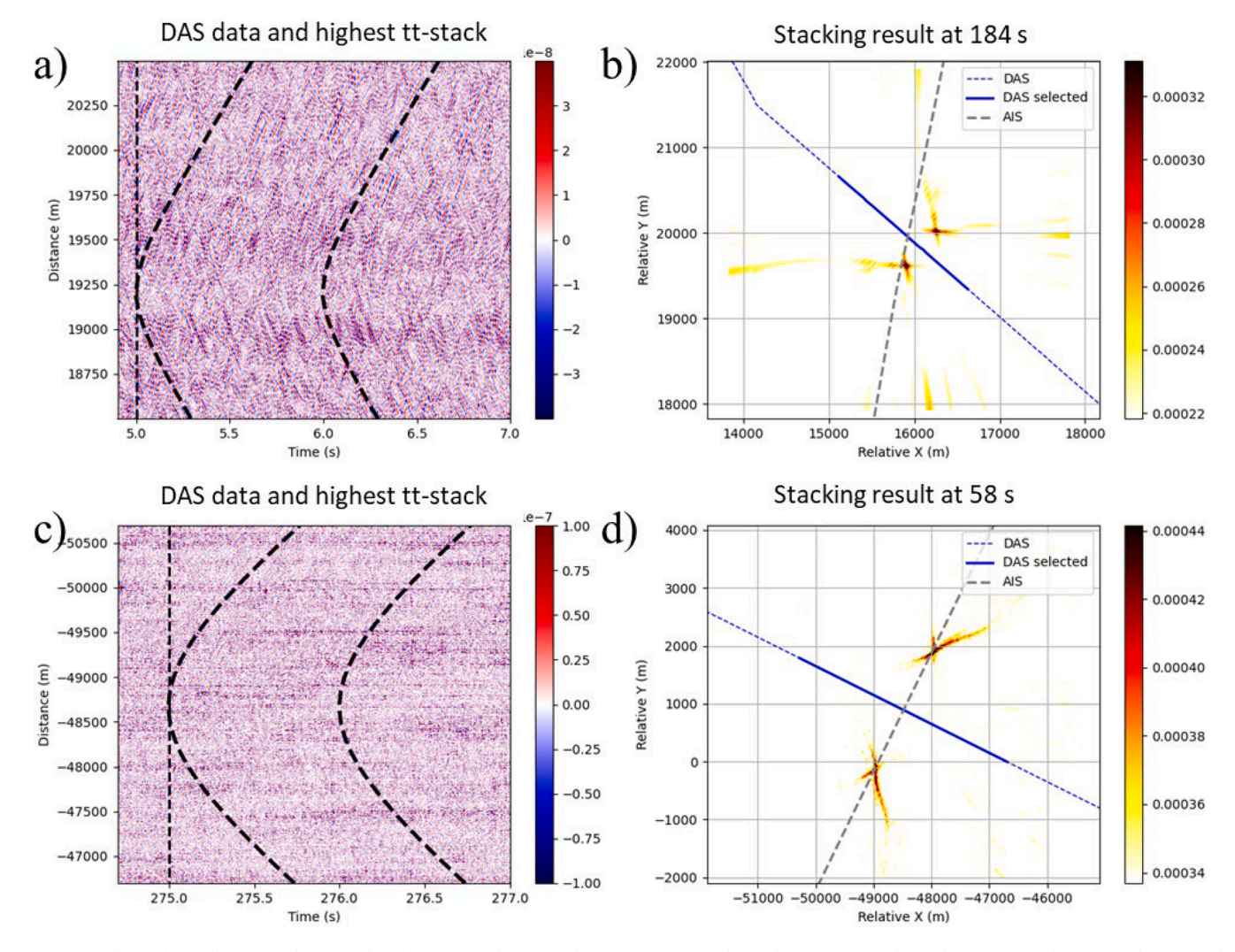


Fig. 8. Examples of the application of location algorithm approach for vessel 2 (LPG) of the North Sea dataset (a, b) and vessel 3 (Cargo) of the Oregon dataset (c, d). (a, c) Block of pre-processed strain rate data together with the travel time curve giving the highest stacked value within the time window marked by the curved black dashed lines. (b, d) Heat map of the stacking results from the location algorithm. The zone with the highest stacking values is assumed to be the most likely location of the acoustic source, which is in our case the vessel. The location of the DAS cable segment selected for corresponding analysis is shown by the straight blue line and the full DAS cable by the dashed blue line. The AIS data is indicated by the grey dashed line. See Tables 2, 3 and for specifications of considered vessels and DAS processing parameters. Note that panel b corresponds to the same snapshot as Fig. 9e (stacking result at 1700 m/s) and Fig. 10f. Panel d corresponds to the snapshot shown in Fig. 10i.

in the analysis.

The results of the application of the migration-based source location algorithm can be visualized as a heat map where high stacking values resulting from the objective function (Eq. (7)), correspond to a possible acoustic source location (also see Fig. 3). In Fig. 8 a and c the two dashed hyperbola indicate the travel time function corresponding to the highest value from the heatmap shown in b and d (dark red/colors). Note the symmetry of the heat map in Fig. 8b and d, which is caused by the inability to distinguish the direction of signal arrival from fiber-optic data, as it is essentially a single-component measurement in the axial direction of the fiber.

After initial testing we selected a larger search area, coarser grid point spacing and longer DAS cable segment (used for processing) for the Oregon case than for the North Sea case, because the vessel considered at Oregon could be sensed at larger distances than the ones considered for the North Sea case. Here, we balanced the choice between grid size and grid resolution to maintain acceptable calculation times for both cases.

Although the performance of the migration-based source location is dependent on several variables (see Eq. (7)), the result appeared to

especially benefit from optimizing the velocity of the upper subsurface layer (v_2 in Fig. 2), which determines the arrival time of the refracted wave. The effect of successively increasing the p-wave velocity of the top layer on the performance of the migration-based source location algorithm is visualized in Fig. 9. Fig. 9a-i show the effect of varying velocity (v_2) on focusing of the source location region on the heat map. Fig. 9j shows the corresponding mean of the 10 highest stacking values resulting from the location algorithm, as a function of velocity (ν_2). This shows a clear peak value around v_2 =1700 m/s corresponding to the heat map depicted in Fig. 9e, that indeed shows optimal focusing of the source location. Similarly for the North Sea tugboat we found v_2 =1700 m/s, which we adopted for further travel time calculations for the North Sea case. For the Oregon case we similarly determined a velocity for the subsurface of v_2 =1550 m/s (see Table 3). Note that the role of the refractive layer (v_2) is more crucial for the North Sea- than for the Oregon case. Due to the small water depths at the North Sea, there is an approximate critical distance of 28 m, whereas for Oregon it is approximately 1728 m (see Table 3). Thus, for the North Sea a major part of the recorded vessel-induced acoustic waves originating in the region around the cable are refracted waves travelling at v_2 , whereas for

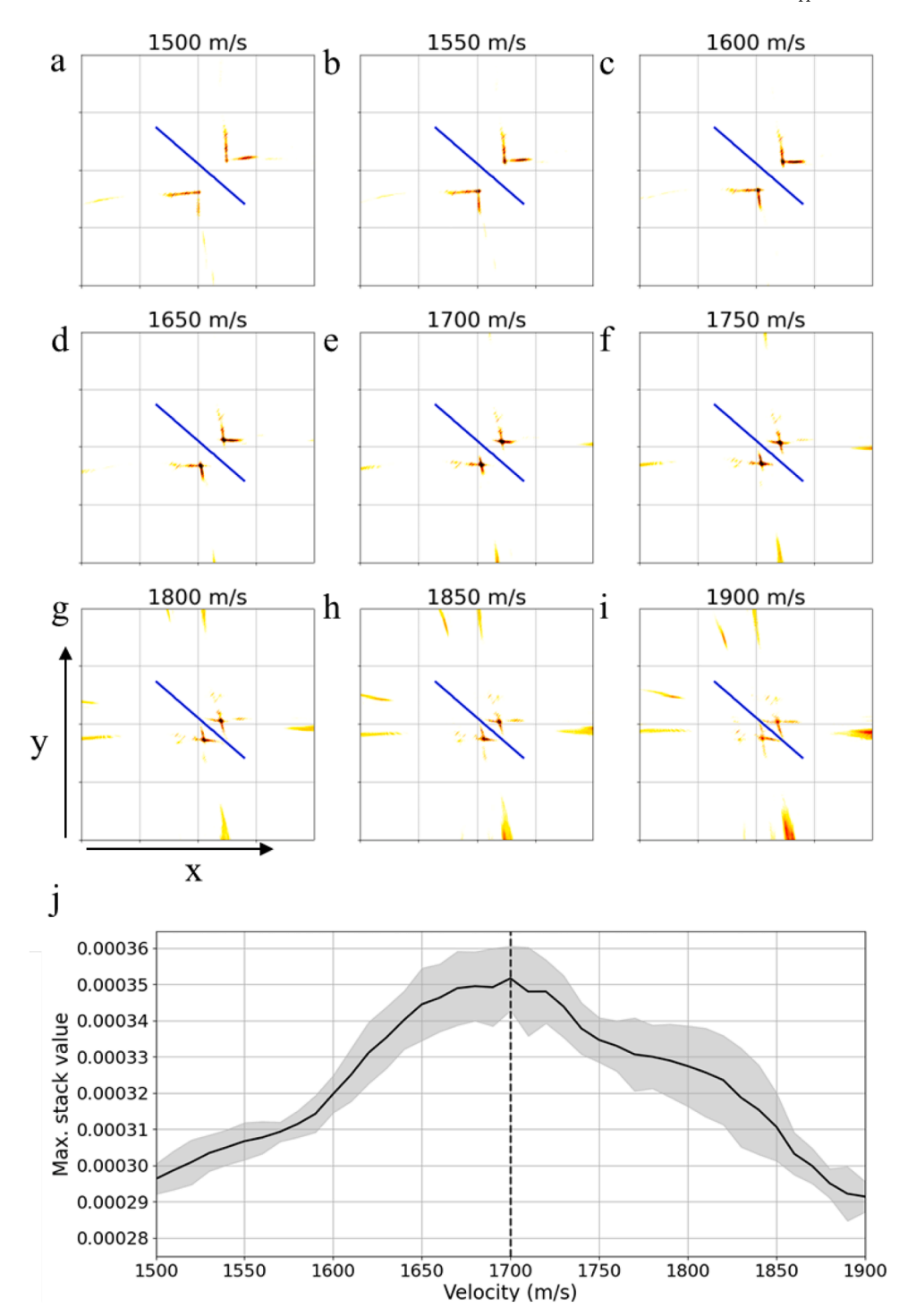


Fig. 9. Effect of velocity of refracting layer on the heat maps obtained from the migration-based source location algorithm. This result is based on the DAS recording of vessel 2 (LPG) of the North Sea dataset (see Table 2). Panels a-i show the effect of different velocities on the migration-based source location outcome visualized as heat map. Panel j shows the mean (solid black) with the standard deviation (shaded grey) of the 10 highest stacking values from the heat map with a peak value around 1700 m/s as indicated by the dashed black line.

Oregon these will mostly be direct waves travelling through the water traveling at ν_1 .

The results of the location algorithm additionally benefitted from increasing the time window used for waveform stacking up to a certain extent. The length of this time window should be constrained by the maximum velocity of the vessels of interest; if the window is chosen too large the synthetic travel times do not adequately fit with the observed ones anymore in the given time window due to waveform phase changes, which will result in destructive interference upon waveform

stacking. Similarly, for the choice of the grid point spacing it is important to make sure travel-time curves calculated on adjacent grid points have limited variation in similarity, such that they adequately capture subtle phase variations of the wavefront as it spreads, assuring constructive waveform stacking in the migration-based source location method.

The migration-based source location algorithm was applied to consecutive data files, encompassing a time frame of several minutes, during which the AIS data reported the presence of a vessel near the

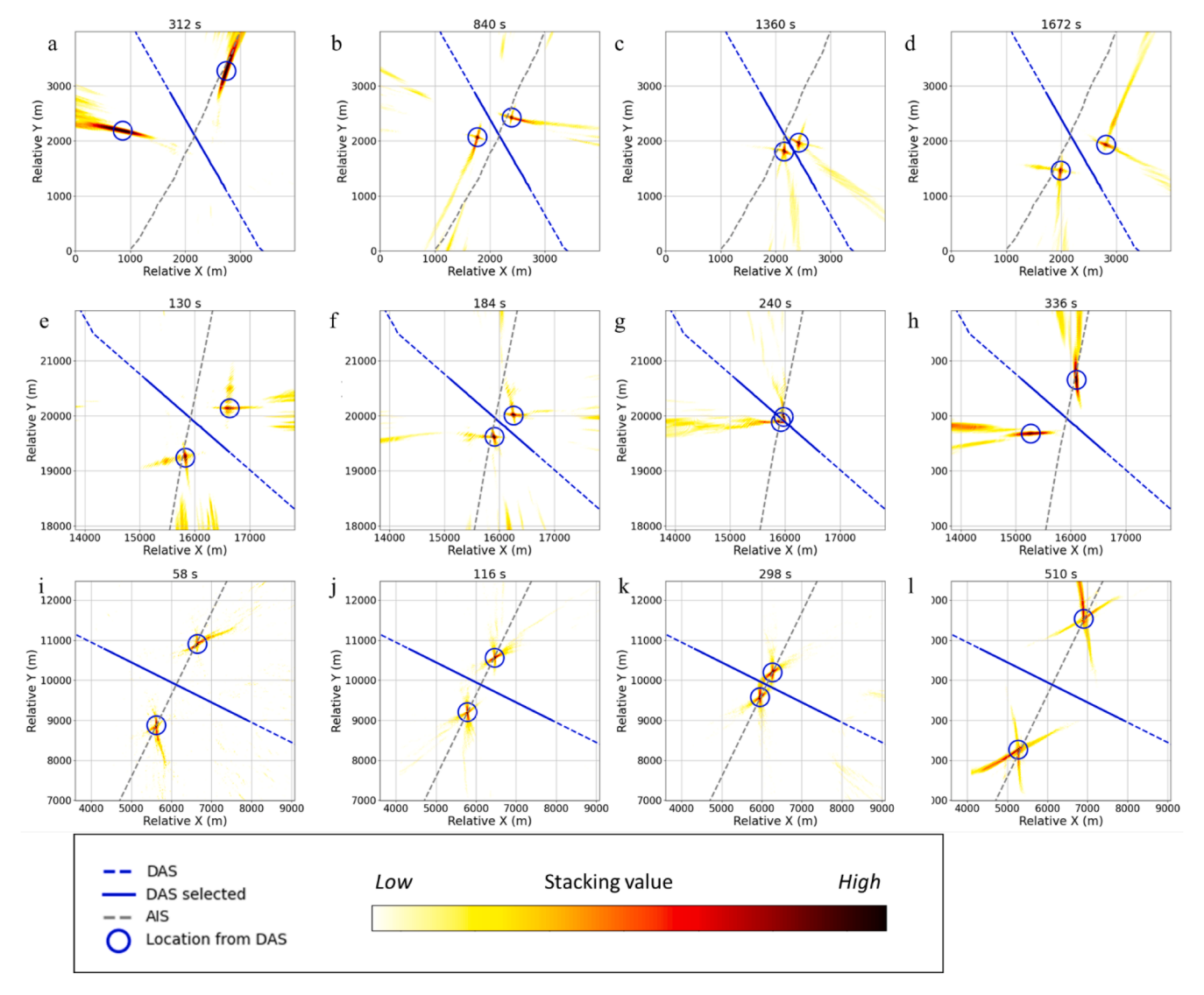


Fig. 10. Results from migration-based source location algorithm visualized as heatmaps for successive times. a–d: Outcome for vessel 1 for the North Sea dataset. E–h: Outcome for vessel 2 for the North Sea dataset. i–l: Outcome for vessel 3 for the Oregon dataset. Dark red to black values correspond to high stacking values. The location of the DAS cable is marked by the dashed blue line, where the solid blue line is the specific DAS segment used in the stacking algorithm to compute the heat maps. The blue circles represent the locations from k-means clustering applied to the 10 highest stacking values, where we impose 2 clusters. See Tables 2 and 3, respectively for specifications of the different vessels and the DAS processing parameters.

cable. Fig. 10 shows successive snapshots of the heatmaps resulting from the location algorithm for the three vessels as they pass over the measurement cable. The blue circles represent the locations determined by applying k-means clustering to the heat maps, which are clearly positioned near the independently reported GPS locations of the vessels (dashed grey line).

The misfit between the vessel locations reported by AIS and the locations based on the location algorithm applied to the DAS data is shown in Fig. 11. To calculate this misfit, we selected one of the two clusters that was positioned closest to the vessel position at the specific time as reported by AIS (i.e. one of the two blue circles in panels of Fig. 10). Note that in the analysis we have chosen to use recorded DAS time series of vessels approximately present within 1.5 km from the fiber-optic cable as shown in Fig. 11. The results are not reflecting the detectability of vessels by DAS, as this depends on many different factors (e.g. vessel types, data quality, data processing). However, the results do illustrate that a fiber-optics based monitoring approach benefits from additional data-processing efforts.

Based on the successive locations found from k-means clustering applied to the heat maps in combination with the time of the recorded DAS files, we also determined the vessel's speed over ground (SOG) and course over ground (COG), which is compared against AIS data in Table 4. For all three vessels, Table 4 shows a clear correlation of the SOG and COG values based on the DAS data and from the AIS data.

Among the different variables analyzed, we observed that both the sediment velocity (also see Fig. 9) and the length of the time window tw used to sum waveforms within the objective function (Eq. (7)) have a significant impact on the locations calculated with our methodology. Fig. 12 addresses how these two variables affect the misfits between AISand DAS derived vessel locations. Here, stacked histogram plots for the misfit are shown for two velocities of the upper sediment layer (Fig. 12a) and 5 different time windows (Fig. 12b) for the LPG vessel on the North Sea, where mean misfits are indicated by the dashed lines. Fig. 12a considers two velocities of the upper sediment layer; $v_2 = 1700m/s$ (green) and $v_2 = 1500m/s$ (light-red). This respectively corresponds to the optimized v_2 based on results of Fig. 9, and the case with $v_2 = v_1$, in which case the refracted sediment wave does not originate due to absence of velocity contrast between the two layers (see Eqs. (1) and (2)). It clearly shows smaller misfits when assuming a sediment velocity of 1700m/s (green) instead of 1700m/s (light-red). This indicates the

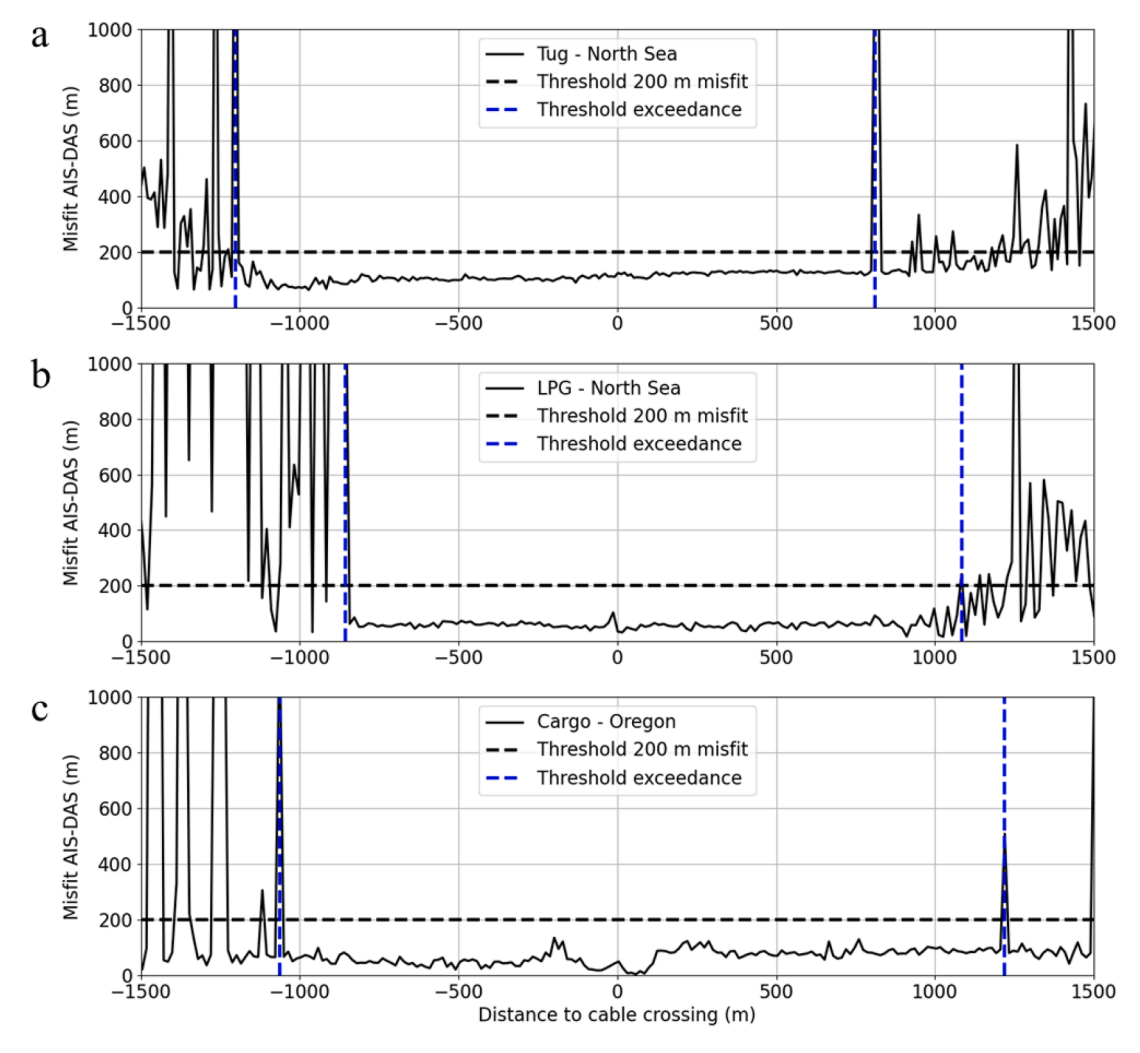


Fig. 11. Misfit between vessel location reported by AIS and the location resulting from DAS data analysis for (a) the tug vessel at the North Sea, (b) the LPG vessel at the North Sea and (c) the Cargo vessel offshore Oregon. The horizontal dashed line marks an offset of 200 m. To calculate this misfit, we selected the cluster closest to the vessel's position at the specific time reported by AIS (i.e., one of the two blue circles in the panels of Fig. 10).

Table 4

Vessel movements based on the results of the stacking algorithm applied to the DAS data. For the three vessels it lists the speed over ground (SOG) and course over ground (COG) reported by AIS data and independently derived from DAS data. The SOG and COG were derived from DAS analysis using the sequence of calculated locations of the vessel sources (e.g. blue dots in Fig. 10) in combination with the UTC times of the DAS files. The COG from the DAS data has two values with a 180° phase shift because of the inability of DAS to discriminate from which side of the cable the signal is arriving. Here we list the azimuth closest to the one reported by AIS.

Dataset	North Sea		Oregon
Vessel type	1. Tugboat	2. LPG vessel	3. Cargo vessel
SOG from AIS (m/s)	1.7	7.2	6.8
SOG from DAS (m/s)	1.5	6.8	6.2
COG from AIS (°)	209.9	12.9	26.0
COG from DAS (°)	202.2	11.6	27.3

importance of adequately accounting for the refracted layer travelling through the sediment, ensuring that observed travel times of coherent events are better represented by synthetic travel times, thereby improving the performance of the migration-base source location method and reducing location misfits. (B). Fig. 12b illustrates how an increase in t_w (from red to green) used within Eq. (7) contributes to smaller misfits between the AIS location and the DAS derived location of

a vessel. This shows that $\mathbf{t}_w=1.0\,\mathbf{s}$, also used as default throughout our analysis gives the smallest misfits, while still being small enough such that vessels remain with grid point distance of 10 m given the speed of the considered vessels.

5. Discussion

The presented data-processing method applied to the considered DAS-data has shown to give robust results with resulting vessel locations confirmed by reported AIS data. The approach highly benefits from the high spatiotemporal- resolution and extent of DAS data by constructively stacking coherent signals both in space and time. The results show that the performance especially increases when adequately accounting for the velocity of the upper sediment layer and by carefully choosing the time window over which data is integrated in the objective function. When employed in a (near) real-time application the presented method can be a valuable tool for detecting and locating acoustic sources in the vicinity of fiber-optic cables pre-existing at the seabed.

The migration-based source location algorithm is expected to further benefit by accommodating (1) the geometrical aspects of the water layer more realistically (tidal variations, wave heights, bathymetry), (2) a 3D layered subsurface model with refined layer- geometries and properties (including cable burial depth) and (3) additional acoustic wave types (e. g. multiples in water and subsurface, deeper reflections, deeper refractions) within travel-time computations. In this way the coherency of

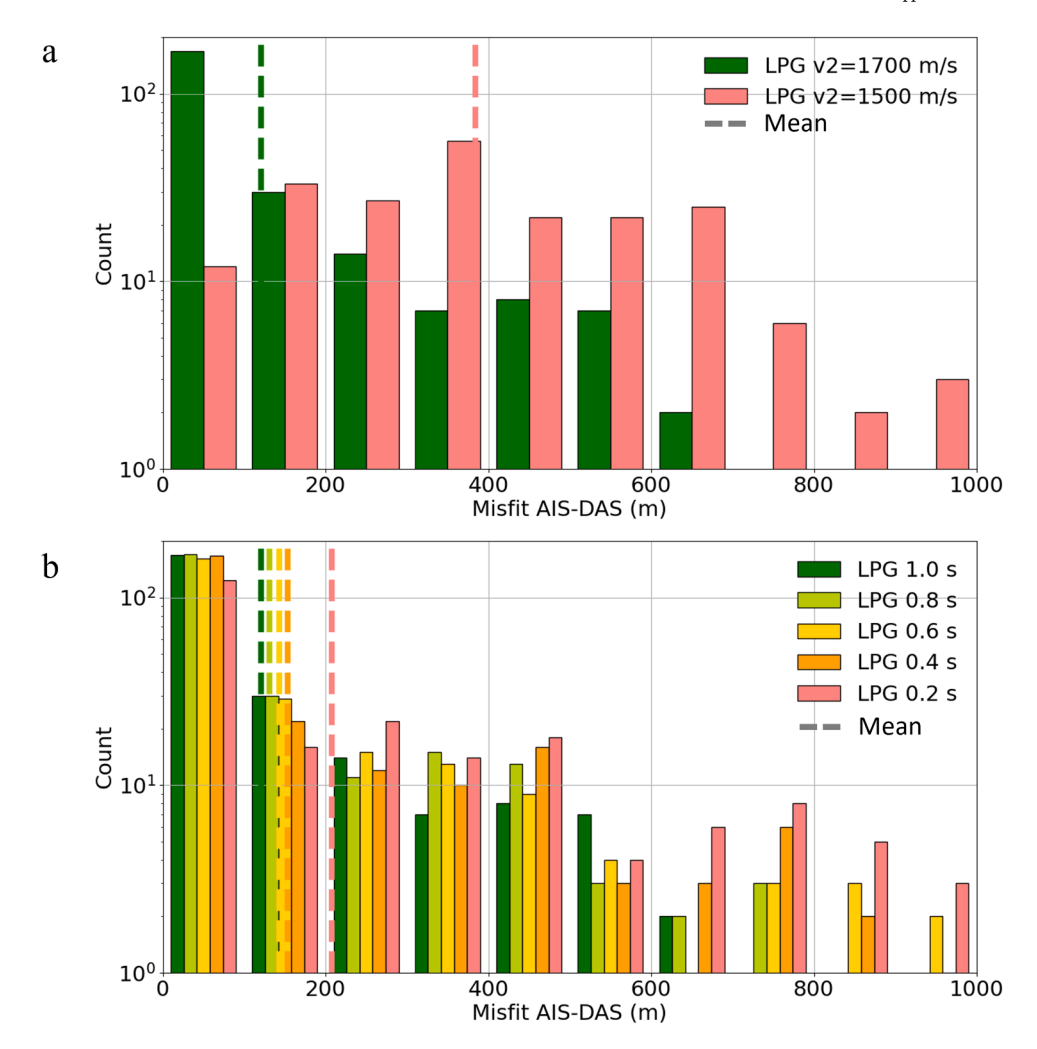


Fig. 12. Stacked histogram plots with misfit between vessel location reported by AIS and the location resulting from DAS data analysis for the LPG vessel at the North Sea, with logarithmic scaling of the y-axis and considering location misfits up to 1000 m. (a) Effect of the velocity of the refracted wave travelling through the sediment layer (\mathbf{v}_2). Here, we consider $\mathbf{v}_2 = 1700 \text{m/s}$ (green) and $\mathbf{v}_2 = 1500 \text{m/s}$ (light-red), respectively corresponding to the optimized \mathbf{v}_2 based on results of Fig. 9, and the case with $\mathbf{v}_2 = \mathbf{v}_1$ where the refracted sediment wave does not originate due to absence of velocity contrast between the two layers (see Eqs. (1) and (2)). In both cases a time window (\mathbf{t}_w) of 1.0 s was used in Eq. (7). (b) Effect of the time window over which the time series is stacked within the objective function (Eq. (7)) on the location misfit. The five histograms ranging from green to red respectively correspond to 1.0 s, 0.8 s, 0.6 s, 0.4 s and 0.2 s window length. For all five cases $\mathbf{v}_2 = 1700 \mathbf{m/s}$ was used. To calculate the misfits in a and b, we selected the cluster closest to the vessel's position at the specific time reported by AIS (i.e., one of the two blue circles in the panels of Fig. 10). The colored dashed vertical lines indicate the mean misfits. Note that the green histograms in a and b) are identical and both correspond to the case where $\mathbf{v}_2 = 1700 \mathbf{m/s}$ and $\mathbf{t}_w = 1.0 \mathbf{s}$.

different observed wave types can be better captured by the calculated synthetic travel-times, which upon waveform stacking will likely result in improved focusing, and a more sensitive and powerful performance of the location algorithm.

Another interesting aspect is the complimentary use of the method to determine the velocity of the upper sediment, where the maximum of the objective function can be optimized by iteratively modifying the velocity model. In this way a preferential velocity model is found where corresponding synthetic travel-times have an optimum fit with the observed travel times resulting in a maximum of the objective function with the best focusing result on the heat map. Thereby it allows for optimization of the velocity model followed by inversion of the acoustic source location, which we demonstrated for a simple two-layer approximation, but that can be extended to a 3D layered subsurface velocity model. In this way vessel-induced acoustic events can be recorded on fiber-optic cables embedded in seabed infrastructure and used to build velocity models in the surrounding of this seabed infrastructure. This local velocity information can in in turn be integrated in regional subsurface velocity models and used for other subsurface studies.

A general limitation of the method where we consider data acquired on a linear array, is its incapability to distinguish from which side a signal arrives with respect to the cable orientation (i.e. directionality effect). This can further be addressed by accommodating fine-scale bathymetric field data in the model representation where local bathymetric asymmetry in the cable surroundings can be used to determine a unique source location. Also, incidental curvature in certain cable segments can help to better constrain the source location. Moreover, the method can benefit by simultaneously monitoring and processing data from neighboring submarine cables that are often aligned within corridors.

We assumed the contribution of different vessel parts to an overall composed acoustic source signal can be simplified as a point source and neglected a vessel-specific acoustic radiation pattern. Especially with shallower water depths (such as the North Sea case) the source-receiver offsets are relatively small, such that the volume where different vibrating vessel parts are present become increasingly significant. Although the point source representation and neglection of the radiation pattern is becoming decreasingly valid in this case, we still observed accurate locations determined by the location algorithm when the vessel

is positioned near or above the cable (at small source-receiver offsets). Nonetheless, more advanced source modelling could help to see if further improvements in the location algorithm may be gained by accounting for a more accurate source representation and corresponding radiation pattern of the vessel.

It was beyond the scope of this research, to determine detection thresholds of various vessels or even classify them from DAS data. This would help to set trigger thresholds on the magnitudes of the acoustic locations found from the algorithm, such that potential false alarms are minimized. Further in-depth research could focus on analysis of DAS data for diverse vessel characteristics and environmental conditions. This includes vessels that differ in various aspects such as size, speed, course, propeller type, and engine specifications. Furthermore, one should consider the effect of various infrastructure types, fiber aspects, interrogator types, water depths and burial depth on recorded DAS data. We foresee that an extensive knowledge database can be built relatively straightforwardly, basically using AIS data to label DAS-data. Machine learning approaches in combination with labelled DAS data in turn may be used complimentary to the migration-based source location algorithm to both locate and classify vessel-induced acoustic events.

6. Conclusions

We successfully applied a processing method to automatically detect and locate vessel-induced acoustic events using two DAS datasets from two types of pre-existing seabed infrastructure, each with different field conditions. The location method consists of a migration-based source location approach and subsequent k-means clustering, and results show a clear correlation between DAS derived vessel locations with the locations from independently reported AIS data. The method makes effective use of the high spatial-temporal density of DAS data through constructive summation of coherent waveforms over space and time. The track, speed and course of the considered vessels could be derived from the analyzed DAS data in the vicinity of the fiber-optic cable and showed consistent agreement with the AIS data. This demonstrates the potential of using DAS measurements to monitor acoustic sources, such as from vessels, in the vicinity of seabed infrastructure. Finally, the method allows for first optimizing the velocity model and then inverting for the acoustic source location in a sequential manner. This highlights the complimentary value of the method for subsurface studies.

Formatting of funding sources

This research did not receive any specific grant from funding agencies in the public, commercial, or not-for-profit sectors.

Data availability

The North Sea DAS dataset cannot be disclosed due to confidentiality reasons. The Oregon DAS dataset is publicly available from Wilcock and Ocean Observatories Initiative (2023).

CRediT authorship contribution statement

Bob Paap: Writing – original draft, Visualization, Methodology, Investigation, Formal analysis, Data curation, Conceptualization. **Vincent Vandeweijer:** Writing – original draft, Project administration, Methodology, Investigation, Data curation. **Jan-Diederik van Wees:** Writing – original draft, Methodology, Formal analysis. **Dirk Kraaij-poel:** Writing – original draft, Methodology.

Declaration of competing interest

The authors declare that they have no known competing financial interests or personal relationships that could have appeared to influence the work reported in this paper.

Acknowledgments

We thank the editor Pengzhi Lin and two anonymous reviewers for their insightful comments which helped to improve the manuscript. We are grateful to FEBUS for giving onsite support to configure the DAS interrogator at the start of the measurement campaign. We thank Kris Hopstaken, Paul Wyers and Tirza van Daalen for their support in managing stakeholder relations throughout this research.

Supplementary materials

Supplementary material S1 includes a movie with results of the location algorithm for the LPG vessel on the North Sea as it crosses over the cable, corresponding to the results depicted in the heatmaps in Fig. 10e-h.

References

- Alvaro, A., Schwock, F., Ragland, J., Abadi, S., 2021. Ship detection from passive underwater acoustic recordings using machine learning. J. Acoust. Soc. Am. 150, A124. https://doi.org/10.1121/10.0007848.
- Anikiev, D., Birnie, C., Waheed, U.B., Alkhalifah, T., Gu, C., Verschuur, D.J., Eisner, L., 2023. Machine learning in microseismic monitoring. Earth Sci. Rev. 239, 104371. https://doi.org/10.1016/j.earscirev.2023.104371.
- Bouffaut, L., Taweesintananon, K., Kriesell, H.J., Rørstadbotnen, R.A., Potter, J.R., Landrø, M., Johansen, S.E., Brenne, J.K., Haukanes, A., Schjelderup, O., Storvik, F., 2022. Eavesdropping at the speed of light: distributed acoustic sensing of baleen whales in the arctic. Front. Mar. Sci. 9. https://doi.org/10.3389/ fmars. 2022. 901348.
- Butcher, A., Hudson, T., Kendall, J., Kufner, S., Brisbourne, A., Stork, A., 2021. Radon transform-based detection of microseismicity on DAS networks: a case study from antarctica. In: Proceedings of the EAGE GeoTech 2021 Second EAGE Workshop on Distributed Fibre Optic Sensing. https://doi.org/10.3997/2214-4609.202131039.
- Cahl, D., Voulgaris, G., Leonard, L., 2023. A comparison of beamforming and direction finding algorithms (Beamscan and MUSIC) on a linear array HF radar in a medium to low wave energy environment. J. Atmos. Ocean. Technol. 40 (2), 191–218. https:// doi.org/10.1175/JTECH-D-22-0005.1.
- Chen, J.S., Dao, D.T., Chien, H., 2021. Ship echo identification based on norm-constrained adaptive beamforming for an arrayed high-frequency coastal radar. IEEE Trans. Geosci. Remote Sens. 59 (2), 1143–1153. https://doi.org/10.1109/TGRS_2020_300903
- Cheng, C.H., Soetaert, K., Borsje, B.W., 2020. Sediment characteristics over asymmetrical tidal sand waves in the Dutch North Sea. J. Mar. Sci. Eng. 8 (6). https://doi.org/
- Chung, K.W., Sutin, A., Sedunov, A., Bruno, M., 2011. DEMON acoustic ship signature measurements in an urban harbor. Adv. Acoust. Vib. 2011 (1), 952798. https://doi. org/10.1155/2011/952798.
- Curilem, G., Vergara, J., Fuentealba, G., Acuña, G., Chacón, M., 2009. Classification of seismic signals at Villarrica volcano (Chile) using neural networks and genetic algorithms. J. Volcanol. Geotherm. Res. 180 (1), 1–8. https://doi.org/10.1016/j. ivolgeores.2008.12.002.
- Dean, T., Cuny, T., Hartog, A.H., 2017. The effect of gauge length on axially incident P-waves measured using fibre optic distributed vibration sensing. Geophys. Prospect. 65 (1), 184–193. https://doi.org/10.1111/1365-2478.12419.
- Doubravová, J., Wiszniowski, J., Horálek, J., 2016. Single layer recurrent neural network for detection of swarm-like earthquakes in W-Bohemia/Vogtland—the method. Comput. Geosci. 93, 138–149. https://doi.org/10.1016/j.cageo.2016.05.011.
- Drylerakis, K.T., Belal, M., Mestre, R., Norman, T.J., Evers, C., 2024. Source detection and tracking for underwater distributed acoustic sensing. In: Proceedings of the 2024 32nd European Signal Processing Conference (EUSIPCO). https://doi.org/10.23919/ EUSIPCO63174.2024.10715378.
- Emodnet, 2025. Bathymetric data. https://emodnet.ec.europa.eu.
- Gan, S., Wang, S., Chen, Y., Qu, S., Zu, S., 2015. Velocity analysis of simultaneous-source data using high-resolution semblance—coping with the strong noise. Geophys. J. Int. 204 (2), 768–779. https://doi.org/10.1093/gji/ggv484.
- Gebco, 2025. Bathymetry data. https://www.gebco.net.
- Gharti, H.N., Oye, V., Roth, M., Kühn, Daniela, 2010. Automated microearthquake location using envelope stacking and robust global optimization. Geophysics 75 (4), MA27–MA46. https://doi.org/10.1190/1.3432784.
- Gibbons, S.J., Ringdal, F., 2006. The detection of low magnitude seismic events using array-based waveform correlation. Geophys. J. Int. 165 (1), 149–166. https://doi.org/10.1111/j.1365-246X.2006.02865.x
- Hartog, A.H., 2017. An Introduction to Distributed Optical Fibre Sensors, (1st ed.). CRC Press. https://doi.org/10.1201/9781315119014.
- Jousset, P., Reinsch, T., Ryberg, T., Blanck, H., Clarke, A., Aghayev, R., Hersir, G.P., Henninges, J., Weber, M., Krawczyk, C.M., 2018. Dynamic strain determination using fibre-optic cables allows imaging of seismological and structural features. Nat. Commun. 9 (1), 2509. https://doi.org/10.1038/s41467-018-04860-y.
- Landrø, M., Bouffaut, L.é, Kriesell, H.J., Potter, J.R., Rørstadbotnen, R.A.,
 Taweesintananon, K., Johansen, S.E., Brenne, J.K., Haukanes, A., Schjelderup, O.,

- Storvik, F., 2022. Sensing whales, storms, ships and earthquakes using an Arctic fibre optic cable. Sci. Rep. 12 (1), 19226. https://doi.org/10.1038/s41598-022-23606-x.
- Lindsey, N.J., Rademacher, H., Ajo-Franklin, J., 2020. On the broadband instrument response of fiber-optic DAS arrays. J. Geophys. Res. Solid Earth 125 (2), e2019JB018145. https://doi.org/10.1029/2019JB018145.
- Malinowski, S.J., Gloza, I., Domagalski, J., 2001. Underwater noise radiated by ships, their propulsion and auxiliary machinery, and propellers. Hydroacoustics 4, 165-168
- Mateeva, A., Mestayer, J., Yang, Z., Lopez, J., Wills, P., Roy, J., Bown, T., 2013. Dual-well 3D VSP in deepwater made possible by DAS. SEG Technical Program Expanded Abstracts 5062–5066. https://doi.org/10.1190/segam2013-0667.1.
- Mestayer, J., Grandi Karam, S., Cox, B., Wills, P., Mateeva, A., Lopez, J., Hill, D., Lewis, A., 2012. Distributed acoustic sensing for geophysical monitoring. In: Proceedings of the 74th EAGE Conference and Exhibition Incorporating EUROPEC. https://doi.org/10.3997/2214-4609.20148800.
- Näsholm, S.P., Iranpour, K., Wuestefeld, A., Dando, B.D.E., Baird, A.F., Oye, V., 2022. Array signal processing on distributed acoustic sensing data: directivity effects in slowness space. J. Geophys. Res. Solid Earth 127 (2), e2021JB023587. https://doi. org/10.1029/2021JB023587
- Rijkswaterstaat, 2025. Geographic data of cables and wind farms in the Netherlands. htt ps://maps.rijkswaterstaat.nl.
- Rivet, D., Cacqueray, B., Sladen, A., Roques, A., Calbris, G., 2021. Preliminary assessment of ship detection and trajectory evaluation using distributed acoustic sensing on an optical fiber telecom cable. J. Acoust. Soc. Am. 149 (4), 2615–2627. https://doi.org/10.1121/10.0004129.
- SEAFOM, 2024. SEAFOM measuring sensor performance document DAS parameter definitions and tests. Report no. SEAFOM MSP-02 V2.0.
- Shen, S., Yang, H., Yao, X., Li, J., Xu, G., Sheng, M., 2020. Ship type classification by convolutional neural networks with auditory-like mechanisms. Sensors 20 (1). https://doi.org/10.3390/s20010253. Article number 253.
- Smith, J.D., White, R.S., Avouac, J., Bourne, S., 2020. Probabilistic earthquake locations of induced seismicity in the Groningen region, the Netherlands. Geophys. J. Int. 222 (1), 507–516. https://doi.org/10.1093/gji/ggaa179.
- Thiem, L., Wienecke, S., Taweesintananon, K., Vaupel, M., Landrø, M., 2023. Ship noise characterization for marine traffic monitoring using distributed acoustic sensing. In:

- Proceedings of the 2023 IEEE International Workshop on Metrology for the Sea; Learning to Measure Sea Health Parameters (MetroSea). https://doi.org/10.1109/MetroSea58055.2023.10317227.
- Tiira, T., 1999. Detecting teleseismic events using artificial neural networks. Comput. Geosci. 25 (8), 929–938. https://doi.org/10.1016/S0098-3004(99)00056-4.
- Vanderkulk, W., Rosen, F., Lorenz, S., 1965. Large aperture seismic array signal processing study. IBM Final Report, ARPA Contract Number SD-296.
- Wang, H.F., Zeng, X., Miller, D.E., Fratta, D., Feigl, K.L., Thurber, C.H., Mellors, R.J., 2018. Ground motion response to an ML 4.3 earthquake using co-located distributed acoustic sensing and seismometer arrays. Geophys. J. Int. 213 (3), 2020–2036. https://doi.org/10.1093/gji/ggy102.
- Wilcock, W., 2023. Ocean Observatories Initiative, 2023. Rapid: a community test of distributed acoustic sensing on the ocean observatories initiative regional cabled array. Distributed Acoustic Sensing dataset. https://doi.org/10.58046/5J60-FJ89.
- Wilcock, W.S.D., Abadi, S., Lipovsky, B.P., 2023. Distributed acoustic sensing recordings of low-frequency whale calls and ship noise offshore Central Oregon. JASA Express Lett. 3 (2), 026002. https://doi.org/10.1121/10.0017104.
- Williams, E.F., Fernández-Ruiz, M.R., Magalhaes, R., Vanthillo, R., Zhan, Z., González-Herráez, M., Martins, H.F., 2019. Distributed sensing of microseisms and teleseisms with submarine dark fibers. Nat. Commun. 10 (1), 5778. https://doi.org/10.1038/s41467-019-13262-7.
- Winder, T., Bacon, C.A., Smith, J.D., Hudson, T., Greenfield, T., White, R.S., 2020.
 QuakeMigrate: a modular, open-source python package for automatic earthquake detection and location. In: Proceedings of the AGU Fall Meeting.
- Withers, M., Aster, R., Young, C., Beiriger, J., Harris, M., Moore, S., Trujillo, J., 1998. A comparison of select trigger algorithms for automated global seismic phase and event detection. Bull. Seismol. Soc. Am. 88 (1), 95–106. https://doi.org/10.1785/BSSA0880010095.
- Yongtan, L., 1996. Target detection and tracking with a high frequency ground wave over-the-horizon radar. In: Proceedings of the International Radar Conference. https://doi.org/10.1109/ICR.1996.573765.
- Zak, A., 2008. Ships classification basing on acoustic signatures. WSEAS Trans. Signal Process. 4 (4), 137–149.